High-performance perovskite solar cells obtained by hybridizing SnS quantum dots with $CH_3NH_3PbI_3$

Liya Zhou (zhouliyatf@163.com)
Guangxi University
Xiaoying Zhong
Guangxi University
Hua Fan
Guangxi University
Jiangying Lu
Guangxi University
Yingjun Ou
Guangxi University

Research Article

Keywords: SnS QDs, hybrid material, perovskite solar cells, photoelectric conversion efficiency

Posted Date: April 21st, 2021

DOI: https://doi.org/10.21203/rs.3.rs-443874/v1

Abstract

In this work, SnS quantum dot (QDs) were added into the $CH_3NH_3PbI_3$ (MAPI) perovskite precursor solution to fabricate MAPI/SnS QDs films with preferred (110) orientation and a perovskite film with large crystal size. This hybrid material showed increased light harvesting ability and a red shift with respect to the number of SnS QDs. As a result, an enhanced performance was achieved in the perovskite solar cells (PSCs) based on MAPI/SnS QDs prepared from the S_5, exhibiting a maximum photoelectric conversion efficiency (PCE) of 10.15%, an open-circuit voltage (V_{oc}) of 1.41 V and a fill factor (FF) of 65%.

Introduction

There have been studies on inorganic – organic hybrid PSCs since 2009, [1–3] initially showing an efficiency of 3.8%. With the in-depth study, PSCs have become a research hotspot, [4–6] and their PCE has improved. Due to the advantages of direct band gap, long carrier lifetime, [7] high optical absorption coefficient, [8] and ambipolar charge transport capability, [9] the lead methylammonium triiodide (MAPI) hybrid perovskites based solar cells has become a promising material for the next generation of photovoltaic devices. As an absorber, since the elemental combinations of perovskite is incorporated into one of the three lattice sites of the general ABX_3 perovskite structure, it possesses excellent optoelectronic properties and versatility. [10–12]

Semiconductors, such as PbS, [13] CuS, [14] and CdS, [15] have been commonly researched in PSC field due to their excellent optical properties. These materials can increase conversion efficiency and are commonly used to fabricate quantum dots (QDs). However, their high toxicity brings adverse effects to living things and the environment, which are inconsistent with the main goal of solar cells as a clean and green energy generator. [16–17] SnS is cheap and less toxic than the above semiconductors, but only a few studies have focused on its application in PSCs. [18] SnS is an IV–VI type semiconductor, with an indirect bandgap of 1.0–1.2 eV and a direct bandgap of approximately 1.3 eV, and its PCE is as high as 25%.[19–21] Owing to its excellent luminescence and photoelectric conversion properties, and the high abundance of Sn and S reserves on earth, SnS has potential application in lasers, detectors, light-emitting diodes, photoconductors, solar cells, commercial sensors, and lithium and sodium ion batteries. [22–24] Yin et al. used a SnS single crystal to study a high- sensity chemo-resistive gas sensor for NO_2 detection at room temperature. [25] A SnS film with large light transmittance and great photoconductivity can accelerate the transmission of electrons in the electron transport layer and reduce the resistance in the process. [26] As an intrinsic p-type semiconductor, SnS has an important characteristic of carrier concentration, so it is useful when forming a type II staggered band alignment with halide perovskite semiconductors. [27–28]

PbS, CdS, and other semiconductor materials are also applied to PSCs but are only currently used as ETLs. Only a few studies focused on the co-sensing of inorganic semiconductor materials and perovskite solar cells. In this study, SnS QDs were incorporated into a perovskite precursor solution, and the performance of the perovskite layer was optimized by adjusting the composition of the precursor

solution. In addition to its contribution to light absorption, SnS incorporation improved the FF and PCE of the PSCs. The compatibility of the Pb in perovskite and the Sn in SnS makes it possible to form high-quality hybrid film. This study provides a valuable strategy to further improve the performance of PSCs.

2. Experimental

2.1 Chemical characterization

All the materials used in the experiment were purchased. Titanium (diisopropoxide) bis(2,4-pentanedionate) (75% isopropanol solution, Macklin) and dyesol-30NR-D; $Na_2S·9H_2O$ (AR, 98%), $SnCl_2·2H_2O$ (AR, 99%) were purchased from Tianjin Damao Chemical Reagent Factory. Conductive glass (FTO), PbI_2 (AR, 99.9%), and CH_3NH_3I were bought from Chengdu Adler Technology Co., Ltd. C_2H_5OH (AR, 99.7%), C_3H_8O (AR, 99.7%), Oleic acid (Aladdin, AR), and NaOH (AR, 96%) were acquired from Guangdong Guanghua Technology Co., Ltd. Carbon paste (NJU-GC) and DMF (AR, 99.5%) were obtained from Kunshan Sunlight Technology Co., Ltd. All experimental procedures were conducted with a controlled ambient temperature of 25°C–35°C and a relative humidity of 60–80%.

2.2 Synthesis Of SNS QDS

Tin sulfide (SnS) QDs were prepared following a previous method. [29] 76 mg of $SnCl_2·2H_2O$ was added to 20 mL of ethylene glycol (EG) and stirred vigorously, and then slowly drip 4 mL of triethanolamine into the mixture. Next, 2 mL of EG solution in 32 mg sodium sulfide (Na_2S) was dropwise injected to the $SnCl_2$ solution. Stir uniformly, the solution was then transferred to a high-pressure reaction kettle and reacted at 180°C for 12 h. Subsequently, the precipitate was collected through centrifugation and washed with anhydrous ethanol and DMF after the temperature decreased to room temperature. Finally, the wet product was directly dispersed in DMF to form SnS QDs.

2.3 Fabrication Of PSCS

An etched fluorine-doped tin oxide (FTO) conducting glass was cleaned with acetone, deionized water, and isopropyl alcohol by ultrasound for 30 min, followed by a 20 minutes of UV treatment. A TiO_2 compact layer was prepared through spin-coating a 1.5 M solution of diisopropyl bis(acetylacetonate) titanate in n-butanol on the FTO surface at 3000 rad/min for 20 s. The spin-coated glass sheet was annealed on the heating stage at 125°C for 10 min. After cooling the glass sheet to room temperature, the anhydrous ethanol solution of TiO_2 slurry was spin-coated on the glass sheet surface at 2000 rad/min for 20 s to form a mesoporous layer. The glass was set again at a heating stage of 100°C for 10 min. The TiO_2-coated base was then put into a temperature programmed oven and annealed at 500°C for 30 min. After 0.462 g of PbI_2 and 0.191 g of MAI were weighed, 1 ml of DMF and SnS solution (5:0, 4:1, 1:1, 1:4, 0:5) was added in a volume ratio. Perovskite precursor solutions were formed by reacting at 85°C for 1 h and labeled as S_1, S_2, S_3, S_4, and S_5. FTO/c-TiO2/m-TiO2 was removed and placed in a heating station at 80°C for 1 min. Spin-coat the perovskite precursor solution at 2500 rad/min for 10 s, and then the

samples were obtained and named as M_1, M_2, M_3, M_4, and M_5. A layer of carbon slurry was applied to the surface of the MAPI film and dried by heating at 100°C for 30 min.

2.4 Characterization Of Samples

The crystal structure of the sample was characterized by CuK radiation (lambda = 1.54060) operating at 40 kV using an X-ray powder diffractometer (XRD, SMARTLAB3KW). The morphology of the perovskite film was analyzed by a scanning electron microscopy (SEM, Hitachi SU8220). A field emission transmission electron microscope (TEM, Tecnai G2 F20) was used to observe TEM images. Optical absorption spectroscopy was measured with a 2600 UV-vis spectrometer. X-ray photoelectron spectroscopy (XPS) was recorded by a photoelectron spectrometer (ESCALAB 250XI+, Thermo Fisher Scientific). The steady-state photoluminescence (PL) of perovskite films was measured using a fluorescence spectrometer (Edin: FLS1000). A solar simulator (Zolix SS150) was used to measure all photocurrent t density − voltage (J − V) characteristics of studied devices under a stable illumination AM 1.5 spectral filter, with an intensity that adjusted for providing 1 sun (100 mW/cm^{-2}).

3. Results And Discussion

TEM images (Fig. 1a) show the successful distribution of SnS QDs in the precursor solution. The histogram of SnS QDs in Fig. 1b indicated that the SnS QDs have a homogeneous distribution with an average diameter of 3.5–4.5 nm. SnS and perovskite belong to tetragonal system and have similar crystal structure; hence, the former becomes the crystal nucleus of the latter's growth. The association of band gap with quantum size is called quantum size effect according to the above experimental results.

The surface morphologies of perovskite films prepared without or with SnS QDs are shown in Fig. 2. The grains observed on MAPI/SnS are quite similar to those in the primary perovskite. Figure 2a shows that the MAPI film fabricated by solution S_1 exhibits smaller crystals with an average size of 200 nm compared with the MAPI films prepared by solutions S_2, S_3, S_4, and S_5. Small perovskite grains indicate many perovskite grain boundaries. These grain boundaries and pores often become the recombination centers of electron holes, thus increasing the recombination probability of carriers, forming leakage currents, and adversely affecting the battery performance.[30] Fig. 2 (b–e) shows that the perovskite prepared by the SnS-doped precursor solution has a large crystal size, uniform film, and few microscopic pin-holes. Figure 2e shows that its largest grain size exceeded 1.5 μm, suggesting that SnS introduction can facilitate the grain growth through controlling the crystallization process. Through improving the crystallinity of the film, the carriers separation, light absorption and transport can be enhanced. Moreover, the interplanar spacing of 2.8 and 3.0 Å in Fig. 2f correspond to the lattice distance of the (111) and (220) crystallographic plane of SnS and MAPI, respectively (see the inset of Fig. 2f). The matched lattice is visible in the interfaces between MAPI and SnS QDs. Therefore, the MAPI/QD hybrid structure is an excellent lattice matching heterostructure.

The XRD pattern of the as-synthesized SnS QDs (black line) displayed the (002), (100), (004), (022), (224), and (115) diffraction peaks that are indexed to the orthogonality herzenbergite phase (JCPDS no.97-007-9129). XRD was used to measure the crystal structure of these samples to study the impact of SnS QDs on the crystallization properties of MAPI layer. The (110), (220), (314), (310), and (400) reflections of the MAPI phase [31–33] are visible at approximately 2θ values of ~13.96°, 28.26°, 32.18°, 40.58°, and 43.08°, respectively (Fig. 3a, red line). When the SnS QDs-modified MAPI precursor was used, the diffraction peak positions were similar to those of the samples prepared with the precursor solutions with different ratios of SnS QDs to MAPI. With the continuous use of SnS QDs, the strengths of the two diffraction peaks of (110) and (220) have enhanced significantly, showing a preferred orientation. Among all diffraction peaks, the highest diffraction intensity (S_5) is almost twice of magnitude higher than the lowest diffraction intensity (S_1). No obvious peaks of SnS QDs or TiO_2 were observed in the films. Figure 3b shows the details of the XRD spectra. The peaks of (110) and (220) exhibited a slight right shift with SnS addition, thus confirming that the SnS in DMF could react with MAPI.

XPS measurement was performed to examine the presence of Sn and S (Fig. 4) at the surface of the SnS/MAPI mixed perovskite. The existence of C, I, N, O, Ti, and Pb elements in the sample can be proved by the XPS full spectra, as shown in Fig. 4a. The S2p and Sn3d core-level spectra of SnS/MAPI are shown in Fig. 4b and c. For Sn, the $Sn3d_{5/2}$ and $Sn3d_{3/2}$ [34] peaks are located at 486 and 495 eV (Fig. 4b), respectively. This finding indicates that the oxidation or reduction of Sn^{2+} was successfully inhibited in the precursor solution. As can be seen from Fig. 4c that the S2p signal occurs in the XPS spectra of the SnS/MAPI-coated TiO_2 film. The S 2p level split into $2p_{3/2}$ and $2p_{1/2,}$ with binding energies of 158.0 and 162.5 eV, [35] respectively. This result is in line with previous reports. The C1s spectra of MAPI and SnS/MAPI are shown in Fig. 4d. Two main peaks in MAPI were found at 284.1 and 285.5 eV, indicating the existence of sp^3C carbon (C – C) and C – O, [36] respectively. However, in SnS/MAPI prepared from $S_{5,}$ these designated peaks for C1s shifted in the direction of high binding energies. The shifts in SnS/MAPbI were due to the increase of electron cloud density around SnS. In addition, the typical peak of the C1s spectrum in the SnS/MAPI sample shifted up to a higher binding energy than that in the MAPI, suggesting that adding SnS QDs to perovskite precursor solution can enhance the performance of these devices.

In terms of the light capturing effect, the film with SnS QDs exhibited a significantly higher absorbance than the original film (see Fig. 5). The pure MAPI shows an absorption onset at approximately 752 nm. By contrast, the materials with SnS/MAPI film prepared by solution S_5 have absorption onsets at approximately 762, implying their red-shifted absorption. Moreover, the SnS/MAPI films have strong light absorption, which is beneficial in increasing the current density. The absorption of the hybrid SnS/MAPI (S_5) was enhanced over the broad range and can be regarded as the co-absorption of SnS and MAPI films. This enhanced optical absorption allowed us to design the advanced hybrid SnS/MAPI device.

The steady-state photoluminescence of the perovskite films with or without SnS QDs is shown in Fig. 6. In terms of PL intensity, it was significantly reduced in the perovskite film added with SnS QDs than it was

in the perovskite film, indicating that the excitons can be rapidly separated from perovskite film and transferred to TiO_2 layer.[37] Given that the films showed similar peak maxima and absorption bandwidths, the significantly reduction in PL intensity is probably due to the quenching effect (improved charge collection) caused by the enhanced electron transfer promoted by SnS.

Table

Samples	$J_{sc}(mA/cm^2)$	V_{oc} (V)	FF	PCE(%)
S_1	7.52	1.11	0.59	4.92
S_2	8.69	1.21	0.58	6.10
S_3	9.19	1.29	0.61	7.23
S_4	10.15	1.32	0.63	8.44
S_5	11.08	1.41	0.65	10.15

Figure 7a shows a simulation of the device structure, including a carbon layer, a perovskite layer, an electron transport layer, and a glass substrate coated with an FTO film from top to bottom, with SnS QDs distributed in the perovskite layer. Using c/m TiO_2 layer as the ETL and a carbon paste film as the counter electrode, inorganic–organic hybrid cells based on different absorber layers prepared from solutions S_1, S_2, S_3, S_4, and S_5 were assembled. Holes and electrons were generated and separated in the MAPI/SnS QD hybrid film as the absorber layer in this PSC structure. The J–V characteristic curve of the PSCs prepared from solution S_1, S_2, S_3, S_4, and S_5 for the analysis of SnS contribution to the photovoltaic performance is shown in Fig. 7b. Table 1 shows a summary of the photovoltaic parameters that obtained from J–V measurement of cells with different absorber layers. Compared with the conventional PSC prepared from the pure MAPI precursor solution S_1, the values of J_{sc}, V_{oc}, FF, and η of the PSC (S_5) were significantly increased from 7.52 mA/cm^2, 1.11 V, 0.59, and 4.92% to 11.08 mA/cm^2, 1.41 V, 0.65, and 10.15%. These results suggested that the addition of SnS QDs can improve the performance of PSCs prepared under ambient conditions.

Electrochemical impedance spectroscopy (EIS) measurement was used to analyze the electron transport and recombination resistance with and without the SnS QDs. Figure 8(a) shows the Nyquist plots of TiO_2/MAPI and TiO_2/SnS/MAPI solar cells prepared by S_1, S_2, S_3, S_4, and S_5. In the Nyquist plots, a typical arc may be associated with the overall charge transfer resistance (R2) in the PSCs [39]. With the increase in SnS QD concentration, the heavy volume of quantum dots increased gradually, and the charge transfer impedance values from the original 96 Ω were markedly reduced to 15 Ω when deposited TiO_2/SnS/MAPI film prepared by S_5. This finding implied the strong suppression of charge recombination. Hence, the hybrid material makes sure of the collected holes quickly transporting to the

external circuit and suppressing the recombination between holes and electrons in PSCs, thereby synergistically increasing Jsc and FF. EIS results explain the enhancement of V_{oc}; the large R2 indicates fast electron back-transfer in the PSCs based on TiO_2/SnS/MAPI.

Conclusion

A series of SnS/MAPI composite materials were in situ synthesized and utilized as absorber layer of PSCs. This hybridization method presents advantages of simple, low cost, and easily controlled, and can be fine-tuned when preparing the hybrid layers of perovskite/QDs with two components in different rates. The perovskite films with SnS QDs exhibit very good properties, as well as enhanced light absorption and high crystallinity. The highest performance PSCs (FTO/TiO_2/SnS QDs-MAPI/Carbon paste) was obtained with SnS QDs/MAPI prepared from solution $S_{5,}$ with a J_{SC} of 11.08 mA/cm^2, a V_{OC} of 1.41 V, a FF of 0.65, and an efficiency of 10.15%. Trough hybridizing SnS QDs and MAPI, the PCE of PSCs was increased by 52% compared with that of a pure MAPI cell. The performance improvement is attributed to the increased absorption intensity in visible region and intense quenching at approximately 786 nm after the SnS QDs were embedded into MAPI. This work provides a general method for the preparation of perovskite/QD hybrid materials with potential application in the design and preparation of other hybrid materials.

Declarations

Declaration of interests

The authors declare that they have no known competing financial interests or personal relationships that could have appeared to influence the work reported in this paper.

References

[1] T. Salim, S. Sun, Y. Abe, A. Krishna, A.C. Grimsdale, Y.M. Lam, J Mater. Chem A, 3 (2015).

[2] Y. Zhao, K. Zhu, J. Phys. Chem. Lett, 5 (2014).

[3] L. Meng, J. You, T.-F. Guo, Y. Yang, Acc. Chem. Res, 49 (2016).

[4] K. Wang, S. Olthof, W.S. Subhani, X. Jiang, Y. Cao, L. Duan, H. Wang, M. Du, S.F. Liu, Nano Energy, 68 (2020).

[5] J.M. Marin-Beloqui, L. Lanzetta, E. Palomares, Chem. Mater, 28 (2016).

[6] J. Leveillee, C. Katan, J. Even, D. Ghosh, W. Nie, A.D. Mohite, S. Tretiak, A. Schleife, A.J. Neukirch, Nano Lett., 19 (2019).

[7] M. Alidaei, M. Izadifard, M.E. Ghazi, 52 (2020).

[8] A.I. Rafieh, P. Ekanayake, A. Wakamiya, H. Nakajima, C.M. Lim, C.M. Lim, Sol. Energy, 177 (2019).

[9] W. Ke, C.C. Stoumpos, J.L. Logsdon, M.R. Wasielewski, Y. Yan, G. Fang, M.G. Kanatzidis, J. Am. Chem. Soc, 138 (2016).

[10] S.A.A. Shah, M.H. Sayyad, J. Sun, Z. Guo, Nano. Mater, 11 (2021).

[11] V.K. Ravi, B. Mondal, V.V. Nawale, A. Nag, ACS omega, 5 (2020), 29631-29641.

[12] S. Rahmany, L. Etgar, ACS Energy Lett., 5 (2020).

[13] F. Hao, C.C. Stoumpos, P. Guo, N. Zhou, T.J. Marks, R.P.H. Chang, M.G. Kanatzidis, J. Am. Chem. Soc., 137 (2015).

[14] G. Seo, J. Seo, S. Ryu, W. Yin, T.K. Ahn, S.I. Seok, J. Phys. Chem. Lett., 5 (2014).

[15] J.-W. Lee, H.-S. Kim, N.-G. Park, Acc. Chem. Res., 49 (2016).

[16] R.D. Harris, V.A. Amin, B. Lau, E.A. Weiss, ACS Nano, 10 (2016).

[17] A. Manjceevan, J. Bandara, Electrochim. Acta, 271 (2018).

[18] F.S. Ghoreishi, V. Ahmadi, M. Samadpour, J. Power Sources, 271 (2014).

[19] R.A. Sabory-Garcia, A.L. Leal-Cruz, A. Vera-Marquina, L.A. Garcia-Delgado, A. Garcia-Juarez, A.G. Rojas-Hernandez, Chalcogenide Lett, 15 (2018).

[20] K.K. Ngoi, H.K. Jun, Green Process. Synth., 8 (2019).

[21] M. Kumar, H.-S. Kim, D.Y. Park, M.S. Jeong, J. Kim, RSC Adv., 8 (2018).

[22] H. Coskun, F.H. Isikgor, Z. Chen, M. Imran, B. Li, Q. Xu, J. Ouyang, J Mater. Chem A, 7 (2019).

[23] A. Schneikart, H.J. Schimper, A. Klein, W. Jaegermann, J. Phys. D: Appl. Phys., 46 (2013).

[24] Y.-H. Kim, D.-T. Phan, S. Ahn, K.-H. Nam, C.-M. Park, K.-J. Jeon, Sens. Actuators, B, 255 (2018).

[25] L. Li, Z. Lou, G. Shen, Adv. Funct. Mater., 28 (2018).

[26] H. Li, J. Ji, X. Zheng, Y. Ma, Z. Jin, H. Ji, Mater. Sci. Semicond. Process., 36 (2015).

[27] B. Wang, B. Li, T. Shen, M. Li, J. Tian, J. Energy Chem., 27 (2018).

[28] G. Xing, N. Mathews, S. Sun, S.S. Lim, Y.M. Lam, M. Grätzel, S. Mhaisalkar, T.C. Sum, Science, 342 (2013).

[29] A.P. Chowdhury, B.H. Shambharkar, S.G. Ghugal, S.S. Umare, A.G. Shende, RSC Adv., 6 (2016).

[30] J.K. Nam, S.U. Chai, W. Cha, Y.J. Choi, W. Kim, M.S. Jung, J. Kwon, D. Kim, J.H. Park, Nano Lett., 17 (2017), 2028-2033.

[31] M.H. Li, H.H. Yeh, Y.H. Chiang, U.S. Jeng, C.J. Su, H.W. Shiu, Y.J. Hsu, N. Kosugi, T. Ohigashi, Y.A. Chen, Adv. Mater., 30 (2018), 1801401.

[32] S. Yang, W. Fu, Z. Zhang, H. Chen, C.-Z. Li, J Mater. Chem A, 5 (2017).

[33] Y. Yun, J.Y. Cho, J. Heo, S. Lee, Appl. Sci. Convergence Technol., 27 (2018).

[34] L. Zhang, H. Rao, Z. Pan, X. Zhong, ACS Appl. Mater. Interfaces, 11 (2019),.

[35] G.K. Veerasubramani, M.-S. Park, J.-Y. Choi, D.-W. Kim, ACS Appl. Mater. Interfaces, 12 (2020).

[36] W. Ke, D. Zhao, C.R. Grice, A.J. Cimaroli, G. Fang, Y. Yan, J Mater. Chem A, 3 (2015).

[37] M. Cha, P. Da, J. Wang, W. Wang, Z. Chen, F. Xiu, G. Zheng, Z.-S. Wang, J. Am. Chem. Soc., 138 (2016), 8581-8587.

Figures

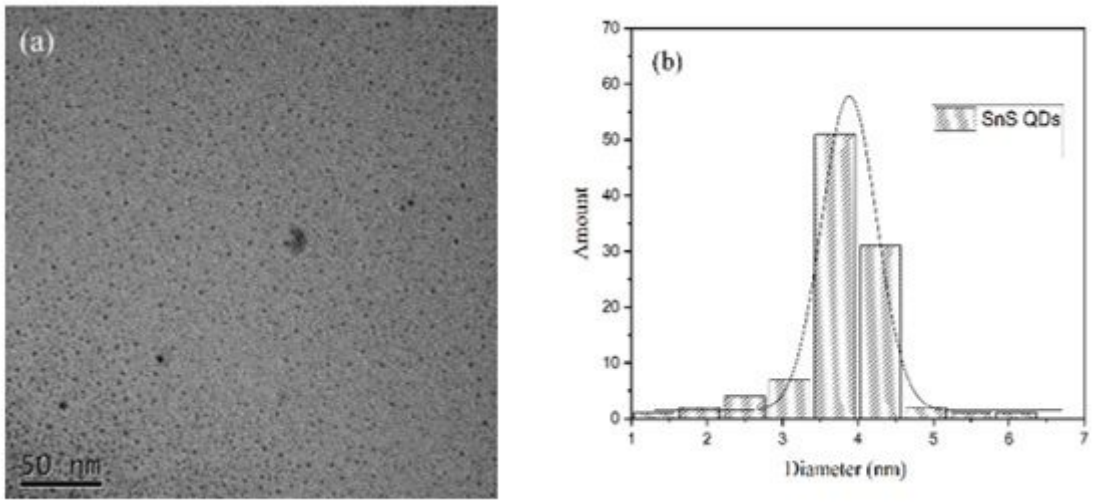

Figure 1

(a) TEM image of SnS QDs (b) the histogram of the size distribution of typical size distribution of SnS QDs distributed in the MAPI precursor solution

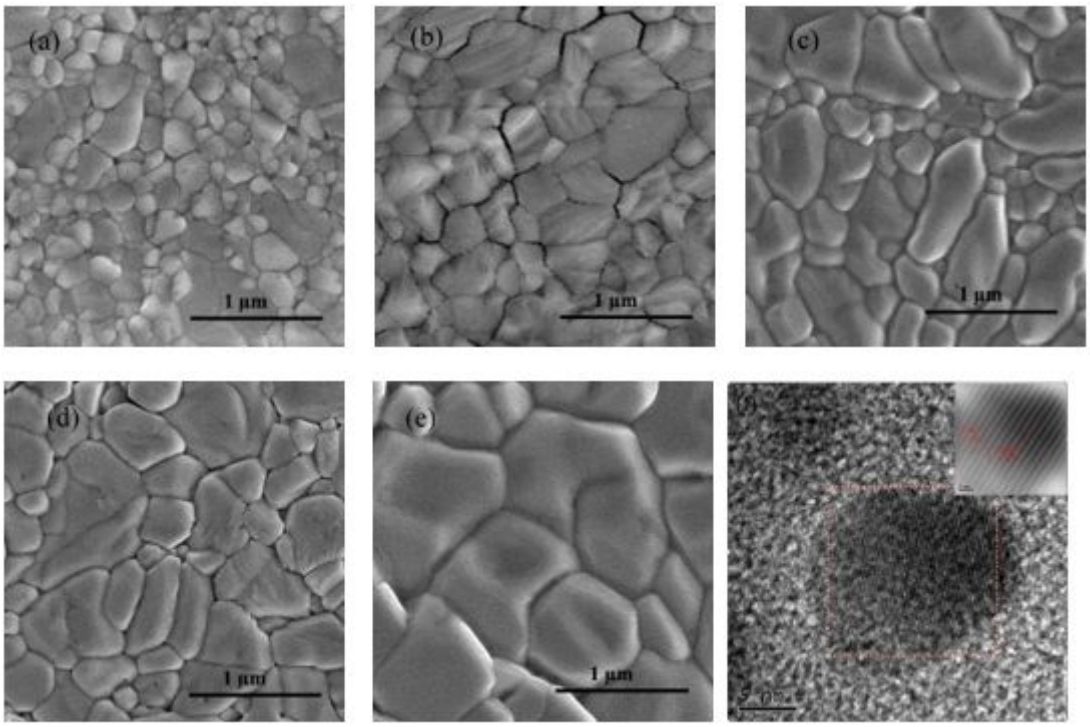

Figure 2

(a-e) Top-view SEM images of the perovskite film prepared from (a) the S1, (b) the S2 (c) the S3 (d) the S4 (e) the S5 (f) HRTEM micrograph of SnS/MAPI prepared from the S5

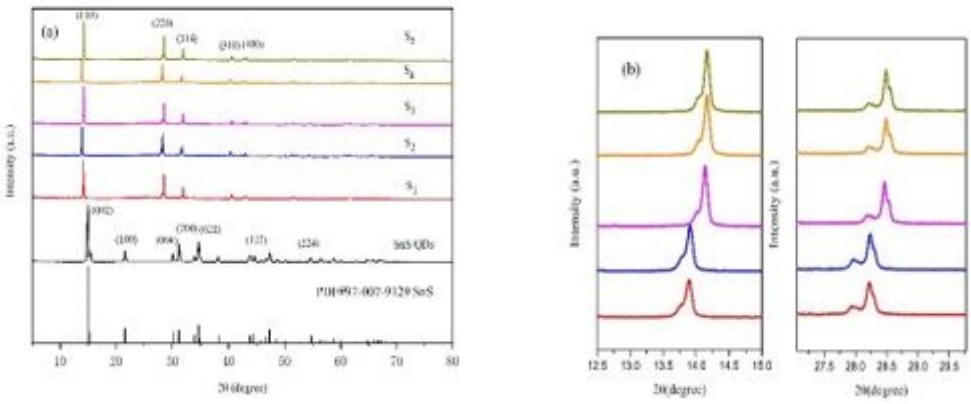

Figure 3

(a) XRD spectrum of SnS QDs and perovskite films prepared by the solutions S1, S2, S3, S4, S5 (b) XRD profiles for (110) and (220)

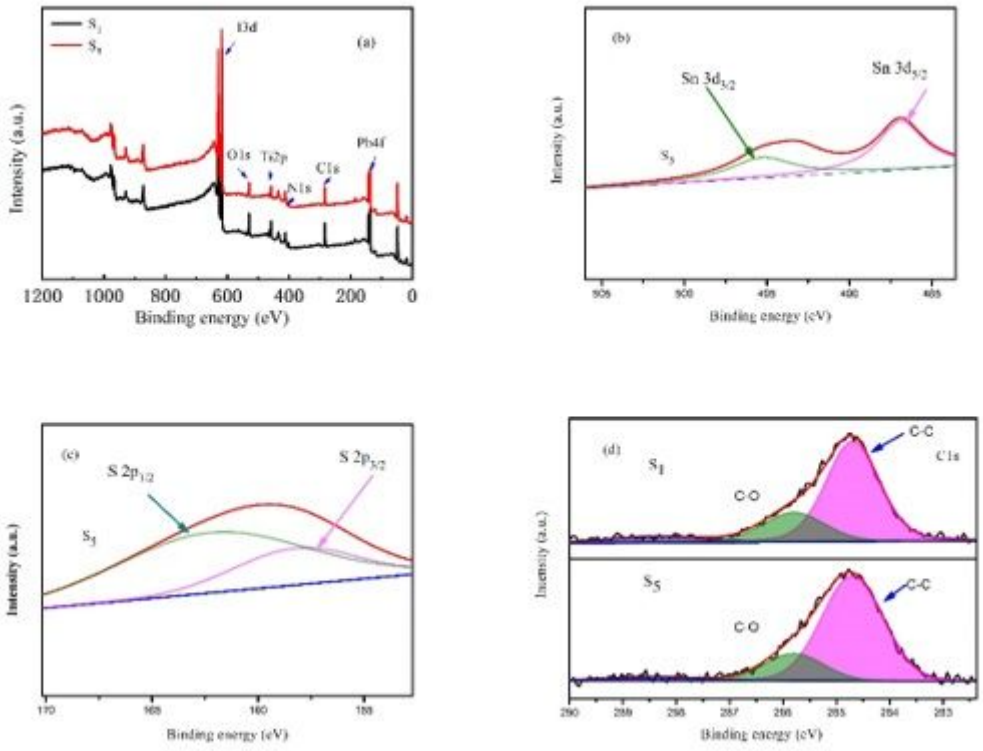

Figure 4

(a) XPS full spectrum of MAPI and SnS/MAPI (b) XPS spectrum of Sn 3d in SnS/MAPI (c) XPS spectrum of S 2p in SnS/MAPI (d) XPS spectra of C1s in the pure MAPI and SnS/MAPI

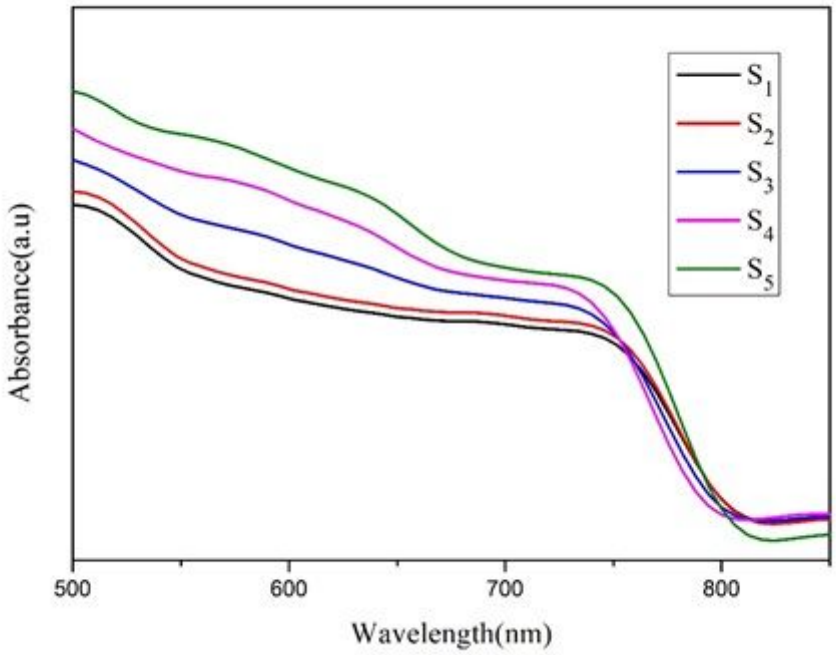

Figure 5

UV-Vis spectrum of perovskite films prepared by the solutions S1, S2, S3, S4, S5

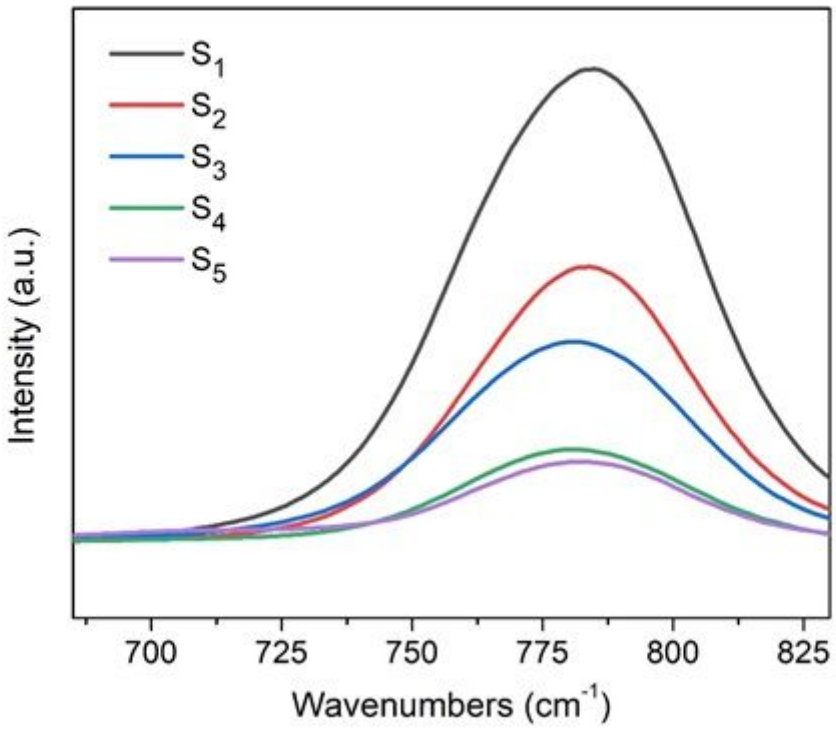

Figure 6

PL spectrum of perovskite films prepared by the solutions S1, S2, S3, S4, S5

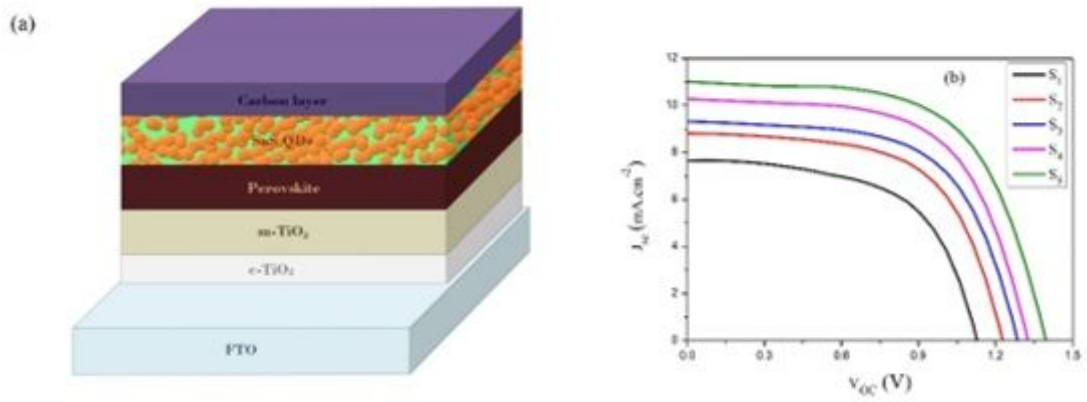

Figure 7

(a) Schematic diagram of the structure of perovskite solar cells doped with SnS QDs, (b) J–V curves of cells prepared by the solutions S1, S2, S3, S4, S5

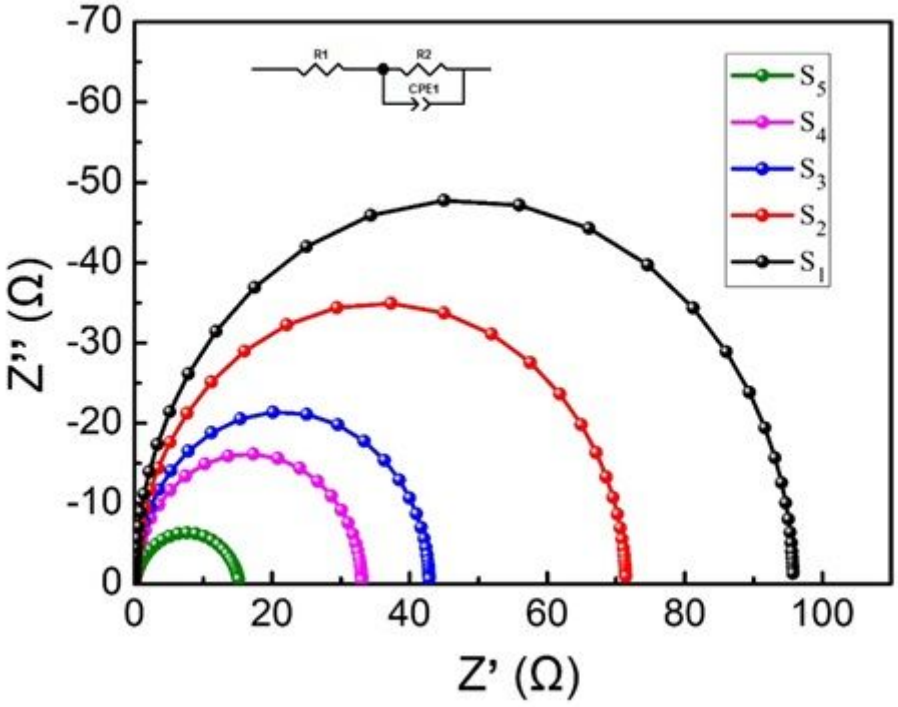

Figure 8

EIS spectra for the cells prepared by the solutions S1, S2, S3, S4, S5